RSC Advances

PAPER

View Article Online
View Journal | View Issue

Cite this: *RSC Adv.*, 2026, **16**, 20715

Recyclable chitosan–biochar biocomposite films for sustainable removal of congo red dye pollutants from water

René Blaise Ngouateu Lekene, *[ab] Mária Kováčová, [b] Christian Brice Dantio Nguela, [a] Matej Mičušík, [b] Alena Opálková Šišková, [b] Anna Vykydalová, [b] Hamed Peidayesh, [b] Daouda Kouotou, [a] Peter Machata, [b] Ndi Juluis Nsami, [a] Angela Kleinová,[b] Julien Parmentier [c] and Zdenko Špitalský [b]

Synthetic dyes, such as congo red (CR), are among the most hazardous pollutants released into aquatic environments due to their toxicity, persistence, and potential health risks. This study prepared and extensively characterized novel chitosan–biochar biocomposite films using SEM-EDS, N_2 adsorption–desorption, FTIR, XPS, TGA, tensile testing, water contact angle measurement, and water absorption and solubility testing to efficiently remove CR dye from aqueous solutions. These characterization techniques revealed that the films exhibited excellent mechanical strength, surfaces enriched with –OH, $-NH_2$, and –COOH functional groups and low porosity. Furthermore, the prepared films could be easily separated from the solution after adsorption. The CR removal percentages of the composites were ~74%, 73%, and 85% for pristine biochar (CH_2BC), acid-modified (CH_2ABC), and base-modified (CH_2BBC), respectively, after 420 minutes with a solution pH of 6.5 at 25 °C. The adsorption data suggested that the kinetic models were those of pseudo-first-order and Elovich models, while the Freundlich model best described the adsorption isotherm. Moreover, CH_2BBC retained up to 79% of its adsorption capacity after four adsorption–desorption cycles, confirming its reusability. The CR adsorption mechanism involves electrostatic attraction, π–π stacking, H-bonding, n–π interaction, imine and sulfone bridging. The environmentally friendly preparation, low cost, and easy regeneration of the prepared chitosan–biochar biocomposite films offer a promising sustainable solution for remediating dye-contaminated water.

Received 10th February 2026
Accepted 14th April 2026

DOI: 10.1039/d6ra01186a

rsc.li/rsc-advances

1. Introduction

Congo red (CR), a synthetic dye, is classified as an anionic diazo dye due to the presence of two –N=N– bonds in its structure. CR has been widely used in various industries for dyeing products such as paper, rubber, textile, and leather,[1] as well as in the formulation of histological stains.[2,3] As the use of CR is constantly increasing, huge amounts of wastewater containing CR are streamed into surface waters, causing its depletion and negatively affecting the aquatic flora and fauna by inhibiting light penetration.[4–6] In terms of its impact on human health effects, CR has been identified as carcinogenic and causes allergic dermatitis and skin irritation.[4] As a result, various techniques have been reported for the treatment of dye-contaminated water, including ozonation, coagulation, chemical oxidation, nanofiltration, electrochemical oxidation, adsorption, and photodegradation.[7–10] Among these techniques, adsorption has been identified as the most convenient method for removing dyes from water due to its low cost, high efficiency, ease of implementation, and the absence of secondary pollution.[9,11] The type of interaction between the adsorbed species and the adsorbent determines which type of adsorption occurs. Chemisorption is a selective process characterized by strong interactions (covalent or ionic) between the adsorbent and the adsorbate, resulting in an irreversible process. In contrast, physisorption involves weak interactions, such as hydrogen bonding, dipole–dipole, van der Waals, and polar interactions. Physisorption is preferred for water treatment due to its nonselective and reversible process.[10,12]

Several adsorbent materials have been used for the removal of dye from water, including metal oxide,[13,14] silica gel, resin, and zeolite,[9] clay,[15] silica, carbon-based materials (activated carbon, carbon quantum dots, carbon nanotubes, graphitic carbon).[12,16] However, they are difficult to use for large-scale applications due to their drawbacks, including poor reusability and high cost. Biochar, an emerging carbonaceous

[a]*Applied Physical and Analytical Chemistry Laboratory, Department of Inorganic Chemistry, Faculty of Science, University of Yaoundé I, P. O. Box 812, Yaoundé, Cameroon. E-mail: blaise.lekene@univ-yaounde1.cm*

[b]*Polymer Institute, Slovak Academy of Sciences, Dúbravská cesta 9, 845 41, Bratislava 45, Slovakia*

[c]*Institut de Science des Matériaux de Mulhouse – IS2M – UMR 7361, Université de Haute-Alsace, 15 rue Jean Starcky, 68057 Mulhouse, France*

material with outstanding physicochemical properties, produced by the pyrolysis of biomass in a limited or oxygen-free atmosphere, has demonstrated its effectiveness in water treatment.[17,18] To further enhance its adsorptive capacity for targeted pollutants, biochar has been modified using several advanced techniques that improve its physicochemical properties.[19,20] Even with its great capacity for removing pollutants from water, recovering and/or regenerating biochar, especially in powder form, can be challenging in practical applications. Once dispersed in water, the powder can become a source of secondary waste. Thus, by extending its lifetime, the disposal of the biochar as a secondary hazardous material is considerably reduced. One solution is to shape the biochar by incorporating it into an appropriate polymer matrix. This could yield a material that not only increases its adsorption capacity but also facilitates its handling, recovery, and reuse after treatment.[21]

Chitosan, a biodegradable and environmentally friendly polymer, has received considerable attention for water treatment due to its nontoxicity and high content of hydroxyl (–OH) and amine ($–NH_2$) groups, which allow strong interaction with various classes of pollutants such as dyes, heavy metals, and other organic/inorganic contaminants has gained significant attention for water treatment.[22,23] However, the use of chitosan is limited by its low mechanical strength and instability in acidic environments, which can be overcome by using cross-linking agents and/or combining it with other materials, such as carbonaceous material, to form composites. In this regard, various chitosan–biochar composites have been used in several studies for the removal of dyes,[24,25] heavy metals,[26,27] nitrate and phosphate ions[28,29] and pharmaceuticals[30,31] from water.

Although the reported studies have demonstrated the efficiency of chitosan–biochar composites for water treatment, most of these studies have focused on using them in powder form. This poses the problem of separation (filtration and/or centrifugation), secondary pollution generation, and reusability after treatment, which significantly increases processing duration and cost. In this study, in addition to its interesting surface functional groups (–OH and $–NH_2$), chitosan was used as a binder polymer for the preparation of biochar film to prevent its dispersion and ensure its environmental application. To the best of our knowledge, there are no studies on using chitosan–biochar composites in the form of films for congo red dye removal from wastewater. Another important aspect of this study is the conversion of agricultural waste into a resource for biochar production. West African countries, including Nigeria, Ghana, the Ivory Coast, and Cameroon, are the main producers of kola nuts. In 2020, more than 300 000 tons were produced.[32,33] Unfortunately, the resulting waste, kola nut shells, is often disposed of untreated in the landfills, causing serious soil and groundwater depletion. Using kola nut shells as the starting material for biochar production could be a good alternative for reducing the environmental footprint. The prepared chitosan–biochar films were easily separated from the solution after the sorption process. They were easily regenerated and could be used for more than five adsorption–desorption cycles. We also investigated the effects of acid/base modification of the biochar surface, as well as the effects of the chitosan/biochar ratio, on the physicochemical, mechanical, and textural properties and adsorption capacities of the resulting biocomposite films towards CR. Finally, we proposed an adsorption mechanism of CR on the prepared biocomposite films.

2. Material and methods

2.1. Reagents

Kola nut shells were obtained from a local farm in Donga Mantum division, Cameroon. Chitosan (degree of deacetylation $\geq$ 80%, average M.W.: 190–310 kDa) from TCI Europe, glutaraldehyde (25%, w/v) from Sigma-Aldrich, congo red from Roth, acetic acid (CH_3COOH), sodium hydroxide (NaOH), nitric acid 65% (HNO_3) from Lachner, hydrochloride acid (HCl), sodium chloride (NaCl), sodium iodide (NaI), sodium sulfate (Na_2SO_4), sodium carbonate (Na_2CO_3), disodium phosphate (Na_2HPO_4), potassium chloride (KCl), calcium chloride ($CaCl_2$), iron(III) chloride ($FeCl_3$), magnesium chloride ($MgCl_2$), barium chloride ($BaCl_2$) were purchased from Centralchem (Bratislava, Slovakia). All the chemicals were used as received. Deionized water (18.2 MΩ cm^{-1}) received from the Millipore Direct-Q3 device was used to prepare solutions.

2.2. Sample preparation

Cola nut shells were washed and sun-dried, followed by pulverization, and the particles with sizes less than 0.8 mm were retained. The obtained particles were pyrolyzed at 500 °C in a muffle furnace (Carbolite Chamber Furnace, Germany) with a temperature rising of 10 °C min^{-1} for 1 hour. After cooling the furnace to room temperature, the biochar was ground, passed through an 80 μm sieve, and stored for further use.[18] To modify the surface properties of biochar, 20 g of biochar was reacted with 200 mL of one molar HNO_3 or NaOH solution under magnetic stirring at room temperature and stored overnight to ensure adequate reaction. Acid and alkaline-modified biochars (ABC and BBC) were washed with deionized water until the pH of the supernatant was stable, followed by oven drying at 80 °C for 12 hours.[25]

The chitosan–biochars films were prepared according to the procedure described by Rizzi *et al.* (2019)[34] with some slight modifications. Briefly, 1% (w/v) of chitosan solution was obtained by dissolving a known amount of chitosan powder in aqueous acetic acid solution (0.8%, v/v) under vigorous stirring for 3 hours at room temperature. Then, 750 μL of glutaraldehyde (cross-linking agent) was added to each 100 mL of chitosan solution, under constant stirring. After 24 hours of stirring the hydrogel solution was filtered with the coarse sintered glass followed by ultrasound sonication for 15 min to remove bubbles. The chitosan–biochars films were obtained by adding 50 or 100 mg of biochars (BC, ABC, or BBC) to 100 mL of chitosan hydrogel solution, followed by ultrasound sonication for 15 min and stirring at 450 rpm for 6 hours. The resulting blackish solution (10 mL) was then cast onto a glass Petri dish (10 cm diameter), oven-dried for 16 hours at 60 °C, and cut into small pieces with an approximate size of 1 cm × 1 cm. Based on the amount and type of biochar added to the chitosan hydrogel

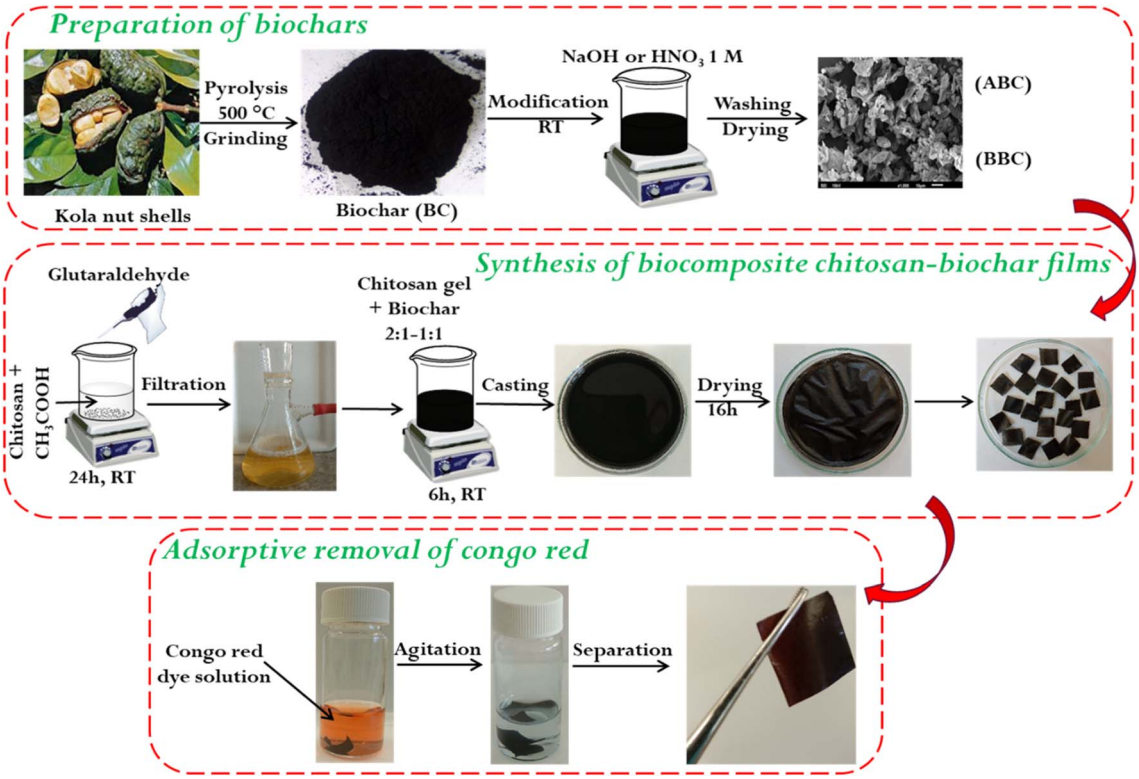

Fig. 1 Diagram of the preparation biochars and biocomposite chitosan–biochar films, adsorption, and simple solid–liquid phase separation.

solution, the biocomposite films were labeled CH_xBC, CH_xABC, and CH_xBBC. Where $x = 1$ or 2 represents the mass ratio of chitosan to biochar. Fig. 1 shows the simplified schematic diagram of the preparation of chitosan–biochar films and their application.

2.3. Characterization

A series of characterization techniques, including SEM, N_2 adsorption–desorption, FTIR, XPS, pH_{pzc}, tensile properties, contact angle, water absorption, solubility in water, and TGA, as described in the SI (S1), were used to evaluate the physico-chemical and mechanical properties of prepared materials.

2.4. Adsorption experiments

All the adsorption experiments were performed in closed reactor by mixing the adsorbent materials and CR solution at a mass to volume ratio of 1 g L^{-1}. A 15 mg L^{-1} CR solution was used for the kinetic studies and was sampled at regular time intervals (10–420 min). The isotherm adsorption experiments were carried out for 24 hours at room temperature in the concentration range 15–340 mg L^{-1}. Kinetic and isotherm studies were conducted at room temperature (RT) and at the natural pH of the CR's solution (6.5). The environmental parameters affecting the adsorption process such as agitation speed (0–320 rpm), pH (3–11), temperature (30–45 °C) leading to thermodynamic studies and interfering anions (Cl^-, I^-, SO_4^{2-}, HPO_4^{2-}, CO_3^{2-}) and cations (Na^+, K^+, Ca^{2+}, Fe^{2+}, Mg^{2+}, Ba^{2+}) were also studied. The pH of the solution was adjusted with a molar solution of NaOH and HCl, while the interfering ions concentration was aligned with that of CR and set at 15 mg L^{-1}.

Only samples containing powder adsorbent (BC, ABC, or BBC) were filtered with a 0.45 μm filter syringe prior to analysis. The CR concentrations in the solution before and after adsorption experiments were evaluated by measuring the absorbance of the solution at a sensitive maximum wavelength of 498 nm (Fig. S1a) using a UV-vis spectrophotometer (Shimadzu UV-1650PC, Japan) based on a pre-established calibration curve (Fig. S1b). The uptake capacity (q_e, mg g^{-1}) and the removal efficiency (R, %) were calculated using the respective following equations:

$$q_e = \frac{(C_0 - C_e)}{m} \times V \quad (1)$$

$$R = \frac{(C_0 - C_e)}{C_0} \times 100 \quad (2)$$

where C_0 and C_e (mg L^{-1}) are the CR concentration before and after the sorption process respectively; V (L) represents the volume of the CR solution; and m (g) is the mass of film.

2.5. Modeling for congo red adsorption

Adsorption kinetic data were analyzed using pseudo-first and pseudo-second order, Elovich, and intra-particle diffusion models, while the adsorption equilibrium data were fitted by Langmuir, Freundlich, and Temkin isotherm models. Thermodynamic data were analyzed using the Gibbs–Helmholtz equation to evaluate the thermodynamic properties of CR

adsorption onto biocomposite films. All models and parameters information are provided in the SI (S2).

2.6. Regeneration and reusability experiments

The reusability of biocomposite films was investigated by four adsorption–desorption cycles using 0.5 mol L^{-1} sodium hydroxide solution as eluent.[1] Initially, biofilm (CH_2BC, CH_1BC, CH_2ABC, CH_1ABC, CH_2BBC, or CH_1BBC) was contacted with a 15 mg L^{-1} CR solution at a ratio of 1 g L^{-1} and agitated at 320 rpm for 24 hours. After adsorption, regeneration was performed by mixing the CR-loaded films with 0.5 mol L^{-1} NaOH solution and agitating for 30 min, followed by extensive washing with deionized water, drying at 60 °C, and using for another adsorption–desorption cycle.

All adsorption and desorption experiments were performed at least in triplicates, and the average values and standard deviations were reported.

3. Results and discussion

3.1. Characterization of materials

3.1.1. SEM-EDS. As shown by the SEM images, the surface morphology of pristine biochar (BC) powder (Fig. 2a) appeared heterogeneous with a mix of particles of irregular shapes and different sizes that did not significantly change after nitric acid (ABC) or sodium hydroxide (BBC) treatment (Fig. 2b and c respectively). However, the small particles considered as impurities were less present on ABC and BBC than on BC. In addition, the (macro)pores present on BC appeared to be obstructed or destroyed on the modified samples due to the etching of the biochar structure. This observation was confirmed by the textural analysis below. Wang *et al.*[35] also found that treating biochar with HCl and H_2SO_4 caused erosion of its surface, a feature that was also observed when activated carbon was modified by NaOH.[36] Uniform coating of the biochar surface by chitosan is observed in the chitosan–biochar composite films (Fig. 2d and e) resulting in passivation of biochar edges and covering of some pores, leading to a decrease in porosity. In addition, the surface of the biocomposite films appeared rough with agglomerates protruding.

Based on the elemental analysis obtained from EDS (Fig. S2, Tables 1 and S1), nitrogen was not detected in any of the analyzed materials. The main contents were C and O, while some alkaline mineral elements (K, Ca, and Mg) were detected. Acid treatment considerably reduces the mineral content in biochar from approximately 3.68% in BC to ~0.96% in ABC

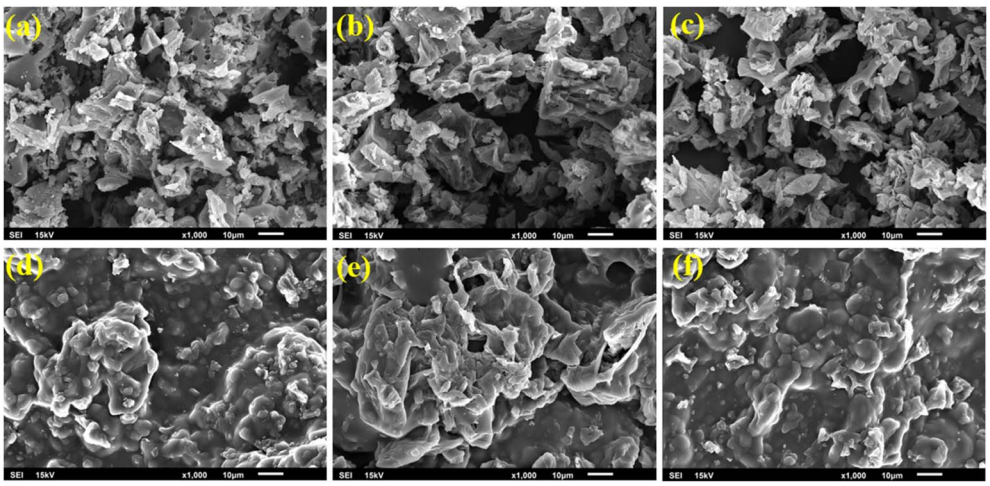

Fig. 2 SEM images of BC (a), ABC (b), BBC (c), CH_2BC (d), CH_2ABC (e), and CH_2BBC (f).

Table 1 Physicochemical properties of biochars and biocomposite films[a]

Samples	C (EDS/XPS) (%)	O (EDS/XPS) (%)	N (EDS/XPS) (%)	Minerals (EDS/XPS) (%)	Specific surface area (m^2 g^{-1})	Pore volume (cm^3 g^{-1})	Pore width (nm)	pH_{pzc}
BC	79.83/75.96	16.49/16.40	n.d./2.32	3.68/5.3	7.542	0.0313	35.450	—
CH_2BC	59.16/62.48	39.04/28.45	n.d./4.54	1.79/4.5	0.731	0.0012	7.203	6.62
CH_1BC	—	—	—	—	1.034	0.0038	7.877	6.63
ABC	74.21/78.03	24.78/17.41	n.d./3.70	0.96/0.9	2.899	0.0077	15.333	—
CH_2ABC	69.32/64.51	30.10/28.99	n.d./5.74	0.57/0.8	0.027	n.a.	n.a.	6.64
CH_1ABC	—	—	—	—	7.075	0.0073	5.653	7.09
BBC	78.00/68.71	17.70/21.70	n.d./2.40	4.30/7.2	2.552	0.0078	21.565	—
CH_2BBC	61.25/62.77	37.00/29.39	n.d./6.07	1.75/1.7	1.255	0.0015	7.722	6.52
CH_1BBC	—	—	—	—	1.949	0.0047	11.973	6.77

[a] n.d. not detected by EDS.

while it increases to ~4.30% in BBC. This finding was supported by the work of Collivignarelli *et al.*[37] On the other hand, the O/C ratios of BC, ABC, and BBC were found to be 0.21, 0.33, and 0.23 respectively, indicating that acid treatment provided more oxygenated groups (–COOH, –OH).[38,39] The finding in EDS elemental composition was not easily comparable to that of XPS since, in the latter, only the uppermost layers (~10 nm) were analyzed and with high sensitivity indicating that the nitrogen is only found on the surface and not within the bulk of the material. Nevertheless, XPS was complementary to EDS. All the biocomposite films exhibited low C and higher O content compared to their respective based biochar indicating successful obtention of biocomposite.

3.1.2. Textural properties. Adsorption–desorption of nitrogen (Fig. S3) indicates that the biochars (BC, ABC and BBC) exhibit a type II isotherm with H3 hysteresis while the composites present a type III indicating a non or macroporosity of the samples.[40] Table 1 shows a significant reduction in the BET specific areas and pore volumes of biochars after acid and base treatments due to the etching or the collapsing of pores. Specifically, there was a significant narrowing of the BJH average pore width, which decreased from 35.450 nm in BC to 15.333 nm and 21.565 nm for ABC and BBC, respectively. This pore size reduction could be attributed to the partial collapse of the internal pore framework due to harsh chemical treatment conditions, and/or the blocking of the existing pores by the newly created oxygen-containing group.[38,39] Whereas in the case of biocomposite films, all textural parameters, including surface area, pore volume, and pore width showed a further decrease except for CH_1ABC, which has a high surface area close than that of BC. This suggests that the biochars were embedded within the chitosan matrix, therefore limiting surface accessibility. Consequently, the poor textural properties of biocomposite films imply that the congo red adsorption mechanism could likely be controlled by surface functional group interactions rather than porosity.

3.1.3. Surface chemistry. The FTIR spectra of biochar before (BC) and after acid (ABC) and alkaline (BBC) modification show similar peaks, differing only in intensity (Fig. 3a). Indeed, after modification, there is an intensification of the peaks located at around 3352, 2927, 2859, 1590, and 1407 cm^{-1} respectively ascribed to the wavenumber of the stretching vibrations of O–H, $–CH_3$, $–CH_2–$, C=O/C=C, and O–C=O bonds,[27,41] respectively. These results are in agreement with elemental analysis, suggesting that the acid/alkaline treatment successfully increased the oxygen-containing groups, which are important in the mechanism of obtaining chitosan–biochar composite.[39,42] Compared to biochar, chitosan displayed many more peaks (Fig. 3b). The peak at 3374 cm^{-1} could be assigned to the vibration of overlapping O–H and N–H bonds, while the peaks at 2941 and 2887 cm^{-1} could be the stretching vibration of C–H bonds methyl and methylene groups respectively.[29] The stretching vibration of the C=O bond of the primary amide appeared at 1644 cm^{-1}, while the band at 1382 cm^{-1} was assigned to the overlapping of $–CH_3$ symmetric angular deformation and C–N stretching. The peak at 1071 cm^{-1} corresponds to C–O stretching in the β(1→4) glycosidic bond.[43,44] In addition to the functions present in chitosan, the composites also exhibit the characteristics of biochars indicating the successful fabrication of biocomposite. On the other hand, the drastic reduction of the intensities of the peaks related to C=O and O–C=O in the composite (Fig. 3b) indicates the coverage of biochar by chitosan and the possible reaction between the carboxylic group on the surface of biochar and the amine function on chitosan as the XPS will confirm.

Full scan XPS spectra indicated that C, O, and N were the primary constituents of BC, ABC, BBC, CH_2BC, CH_2ABC, and CH_2BBC (Fig. S4). The higher content of oxygenated carbons (C–O, C=O, and O–C=O) of ABC and BBC compared to BC (Tables 1 and S2) indicated successful acidic/alkaline biochar oxidation consistent with EDS and FTIR analysis. In all the biocomposites, there is an increase in the proportion of N 1s and O 1s and a decrease in C 1s which may be due to the surface exposure of many nitrogen/oxygen-containing groups (Table S2),[45] further confirming the biocomposite formation. The peak of Na 1s detected on the spectra of BBC and CH_2BBC (with low

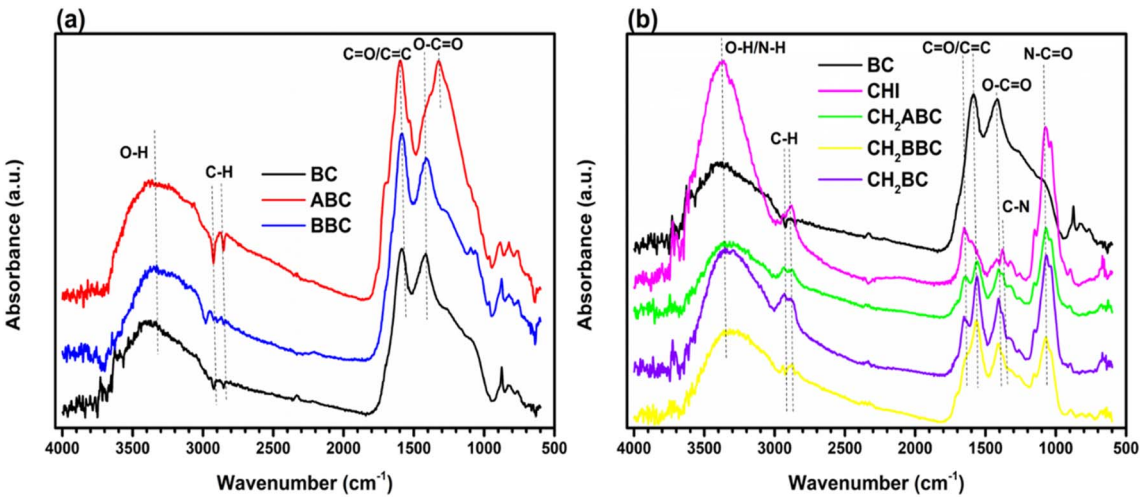

Fig. 3 FITR spectra of biochars (a) and biocomposite films (b).

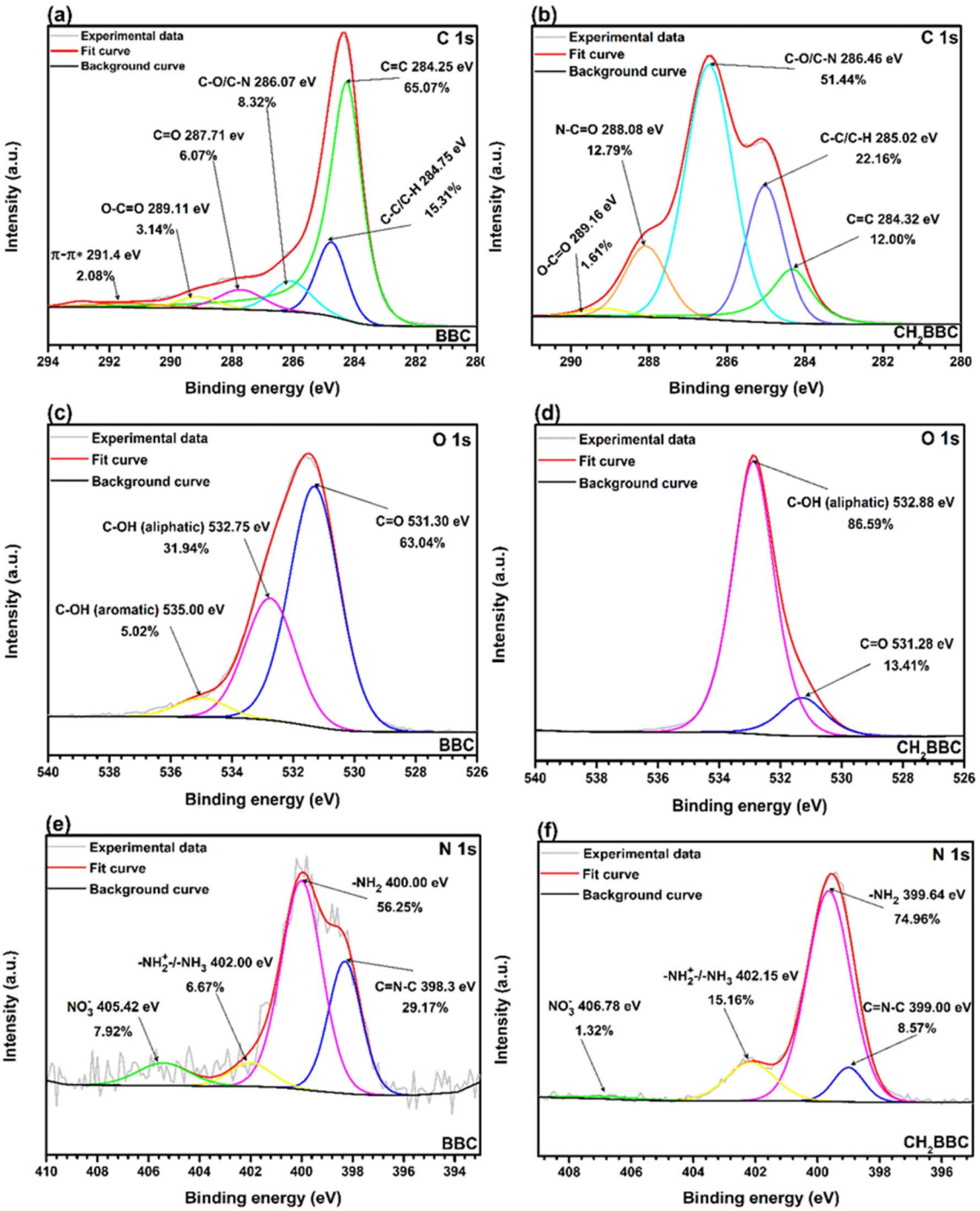

Fig. 4 Deconvoluted XPS spectra of C 1s (a and b), O 1s (c and d), and N 1s (e and f) for BBC and CH_2BBC.

intensity) (Fig. S4) may be due to the introduction of Na^+ during the NaOH treatment which reacted with –COOH to form –COONa.[25] The deconvoluted C 1s spectrum of BBC showed that it has the characteristics of graphitized/graphenized materials containing nitrogen with six peaks (Fig. 4a) centered at 284.75 (C–C/C–H), 284.25 (C=C), 286.07 (C–O/C–N), 287.71 (C=O), 298.11 (O–C=O), and 291.40 (π–π* satellite) eV.[26,46,47] In the spectra of the biocomposite (Fig. 4b), there is the disappearance of a π–π* peak and the formation of the N–C=O bond (288.08 eV). In addition, there is an increase in the percentages of C–O/C–N (from 8.32 to 51.44%) and C–C/C–H (from 15.31 to 22.16%) accompanied by peak shifts, indicating that interactions occurred between BBC and chitosan.[27] In the O 1s spectra of BBC, three peaks were present at 531.30 eV (C=O, 63.04%), 532.75 eV (aliphatic –OH, 31.94%), and 535.00 eV (aromatic –OH, 5.02%) (Fig. 4c), whereas in CH_2BBC (Fig. 4d), we noticed the disappearance of the latter peak and significant increases in the proportion of aliphatic –OH (86.59%), respectively,

attributed to the surface coverage of BBC by chitosan and the abundant presence of hydroxyl on this latter.[25,48] Deconvolution of the N 1s spectrum of BBC (Fig. 4e) revealed four peaks at 398.3 eV (29.17%), 400.00 eV (56.25%), 402.00 eV (6.67%), and 405.42 eV (7.92%) assigned to C═N–C, $-NH_2$, $-NH_2^+-/-NH_3^+$ and nitro ($-NO_2$) respectively, while, these peaks shifted slightly and changed considerably in intensity on CH_2BBC (Fig. 4f).[26,49] The results of XPS were in agreement with those of FTIR.

3.1.4. Thermal analysis. The results of the thermal analysis showed that biochar samples exhibited greater thermal stability and a sluggish decomposition process over temperature (30–950 °C), resulting in a residual percentage of 67.34, 62.98 and 62.33% for BC, ABC, and BBC respectively (Fig. 5a). The reduction of residuals of modified biochar compared to pristine one may be attributed to the liberation at high temperature of oxygenated functional groups introduced after acid/base treatment.[37] In the case of chitosan and biocomposite films, two stages of decomposition were observed. In the first stage, a sharp weight loss between 30 and 110 °C was attributed to the evaporation of adsorbed water, while in the second stage (210–333 °C), the significant weight loss is mainly due to the decomposition of chitosan.[18] Furthermore, in the second decomposition stage, the weight loss in biocomposites started earlier than in chitosan, indicating that the biocomposites are less stable than chitosan at relatively low temperatures, confirming the successful obtaining of biocomposites.

3.1.5. Mechanical properties. The mechanical properties of the prepared biocomposite film samples are given in Fig. 5b and S5. Tensile strength (0.98–5.16 MPa) and Young's modulus (753–900 MPa) decrease to some extent when the amount of biochar increases in the samples made from modified biochar (CH_xABC and CH_xBBC), while the opposite is observed in the case of unmodified (pristine) biochar (CH_xBC). On the other hand, the same trend (increase) is observed for composites based BC and BBC for the elongation at break (1.12–3.94%). All these observations are mainly attributed to the surface chemistry of the different biochars. The more oxygenated groups there are present on the surface of the biochars, as shown by FTIR, XPS, and EDS results, the more interactions there are between the latter and the amine groups present on the chitosan, thus enhancing the mechanical properties of the composite through the formation of hydrogen bridges.[50,51] On the other hand, a large amount of biochar in the biocomposite weakens it by forming aggregates resulting in more or less brittle film.[51] Overall, the good flexibility and rigidity of the prepared films enable them to withstand the effects of agitation

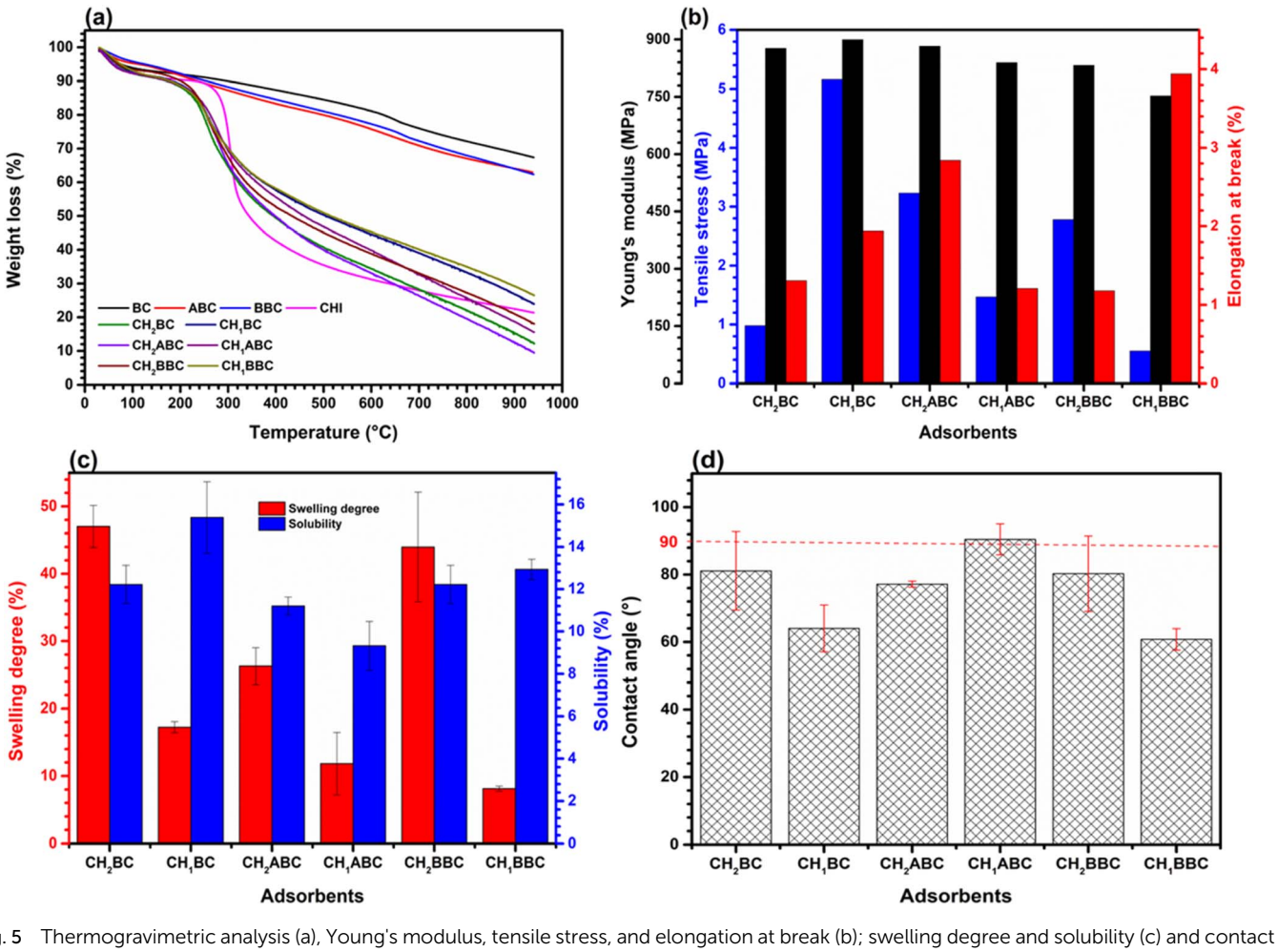

Fig. 5 Thermogravimetric analysis (a), Young's modulus, tensile stress, and elongation at break (b); swelling degree and solubility (c) and contact angle (d) of biocomposite films.

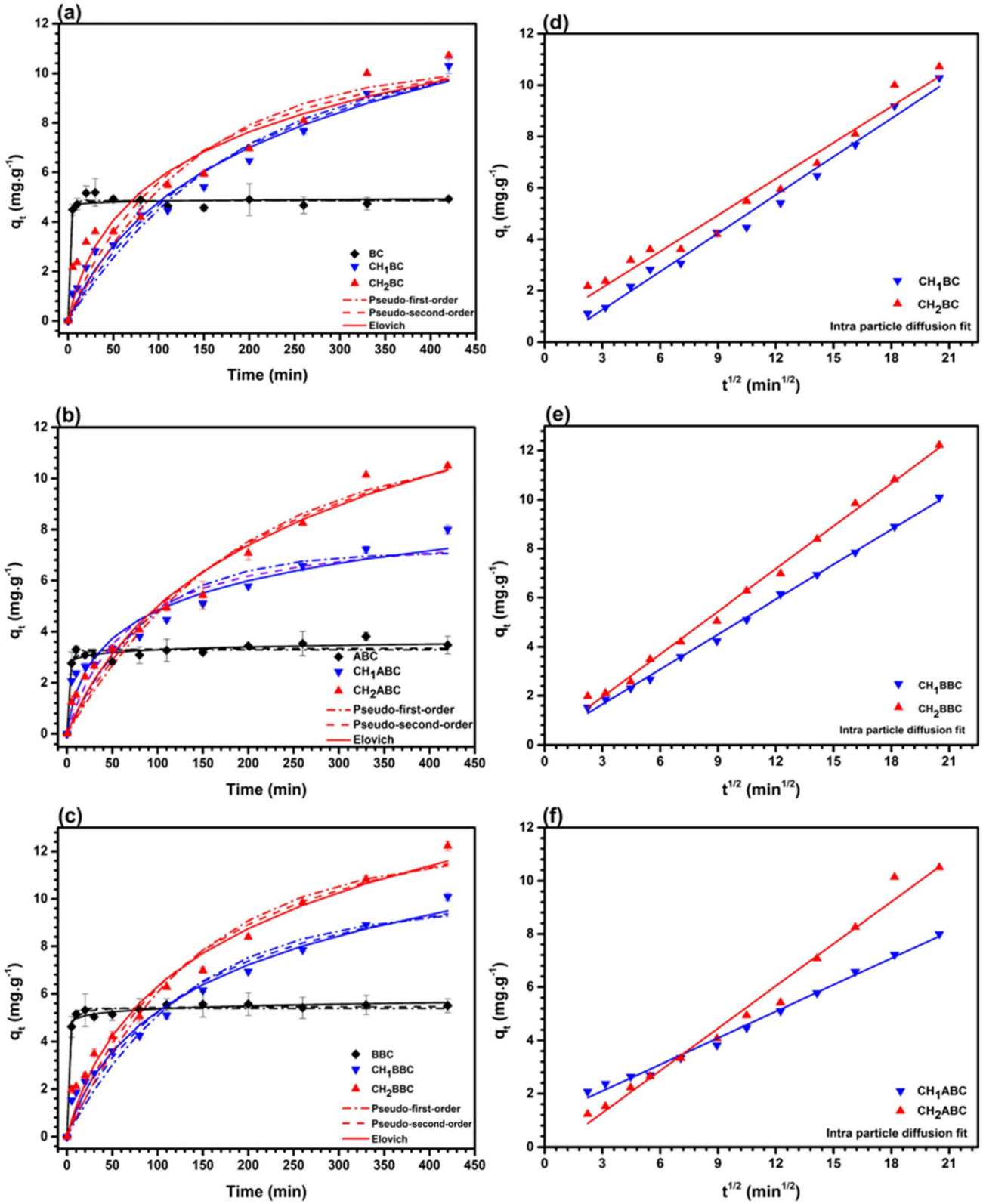

Fig. 6 Adsorption kinetic ($[CR]_0 = 15$ mg L^{-1}, RT, pH 6.5, 240 rpm); pseudo-first-order, pseudo-second-order, and Elovich kinetic model (a–c), intraparticle diffusion fitting model (d–f).

even at high speed and facilitate phase separation after adsorption, thereby allowing for multiple cycles of recycling and reuse.[52]

3.1.6. Swelling, and dissolution of the biocomposite. The swelling performance was affected by the ratio of chitosan to biochar. The swelling degree was higher in the samples containing less amount of biochar. The swelling degree reached 26, 44, and 47% for CH_2ABC, CH_2BBC, and CH_2BC, respectively (Fig. 5c). This may be due to the penetration of water molecules into the chitosan matrix by forming H-bonds with amino and hydroxyl groups, which later leads to their protonation, and therefore inducing an electrostatic repulsion between the positively charged functions.[27,53] On the other hand, as the amount of biochar in the biocomposites increases, there is a decrease in the swelling degree due to the decrease in free amino and hydroxyl groups of chitosan due to their involvement in the formation of hydrogen "bridge" between biochar and chitosan molecule. A high swelling degree of the film is important as it may allow the dye to reach the adsorption sites.[52]

For BC- and BBC-based biocomposites, the solubility (dissolution) slightly increased with the amount of biochar, while the opposite was observed for ABC-based films (Fig. 5c). As shown by EDS results, ABC possessed a more oxygenated group which can strongly react with amine groups of chitosan, and contributed more to the reduction of the solubility of CH_1ABC than CH_2ABC. Nevertheless, the solubility of the films did not exceed 16%, indicating that they can be reused during many adsorption–desorption cycles.

3.1.7. Water contact angle. The water drop procedure was used to assess the contact angle (CA) and examine the wettability of the prepared films, which depend on their morphology (roughness) and surface chemistry.[54,55] The average CA was found to be less than 90° (except that of CH_1ABC) (Fig. 5d and S6), indicating that the film surfaces have hydrophilic features. For the BC and BBC-based films, the wettability increases (decrease of CA) with the amount of biochar, which could mainly be attributed to the increase in surface roughness as reported by Kwaśniewska *et al.* (2021).[54] Moreover, the presence of hydrophilic surface functional groups, such as $-NH_2$ and –OH contributes to an increase in the wettability of the materials. The reverse trend is observed in ABC-based biofilms with the sample CH_2ABC, which is hydrophobic (CA > 90°).

3.2. Adsorption of congo red onto biocomposite films

3.2.1. Adsorption kinetics studies. The influence of contact time on the adsorption of CR by the prepared adsorbent materials is displayed in Fig. 6. All the biochars (BC, ABC, and BBC) reach their adsorption equilibrium within the first 50 min with removal percentages of ~33%, 19%, and 35% for BC, ABC and BBC, respectively. The low removal percentage of biochars may be due to the low presence of surface functional groups necessary for the sequestration of CR. In the case of chitosan–biochar composites, although the rate of the adsorption process was significantly delayed, they exhibited high removal percentages as the amount of chitosan in the composite increased, reaching ~74%, 73%, and 85% for CH_2BC, CH_2ABC, and CH_2BBC, respectively after 420 min, which were significantly higher than that of their respective starting biochars. The high adsorption capacities of the composite films are mainly attributed to the high occurrence of $-NH_2$ and –OH functions (as shown by FTIR and XPS analyses) brought by the chitosan, which are deeply involved in the CR adsorption mechanism. These observations suggest that composite films with the highest chitosan content may be suitable for CR removal with

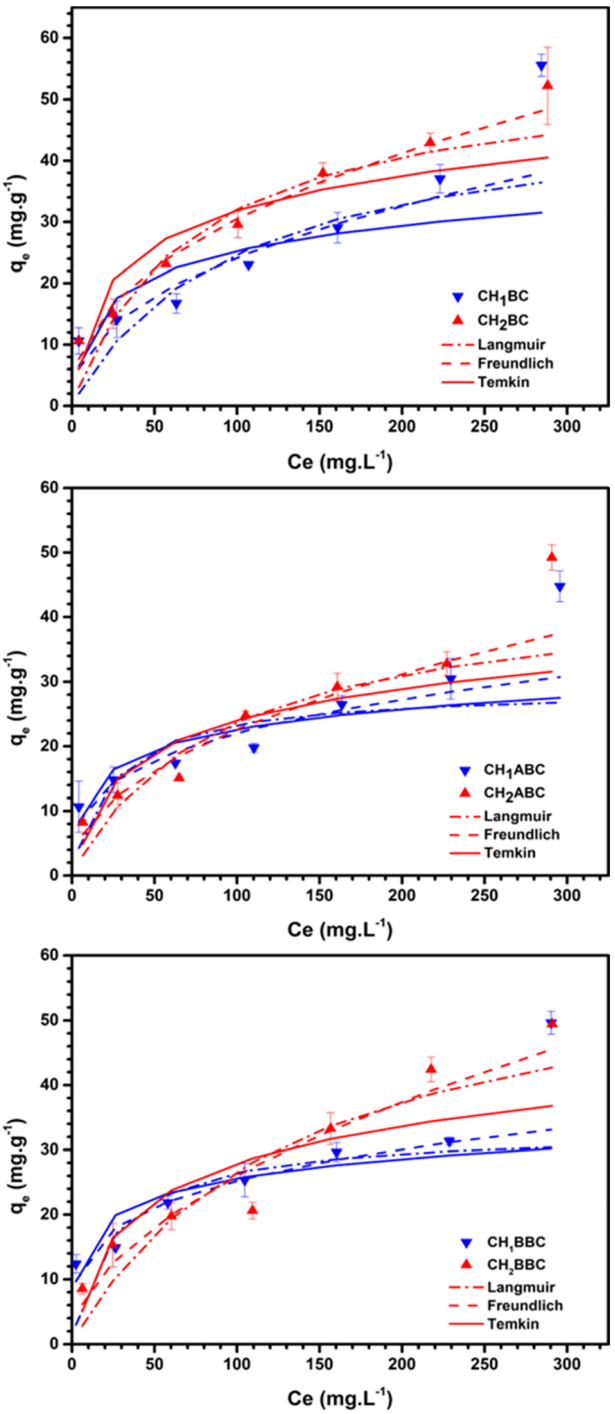

Fig. 7 Adsorption isotherms (RT, t = 24 h, pH 6.5, 320 rpm).

an emphasis on CH_2BBC, which displayed the highest removal percentage.

Pseudo-first-order, pseudo-second-order, and Elovich models were used to fit the adsorption kinetics data of CR (Fig. 6a–c), and the corresponding fitted parameters are given in Table S3. The kinetics data of ABC and BBC were well fitted by the pseudo-second-order and Elovich models, while the pseudo-first-order and Elovich models were suitable for BC according to their high values of R^2 and low values of RMSE and χ^2, indicating that the adsorption process is governed by the chemisorption on heterogeneous surfaces. Indeed, the calculated values of q_e from the pseudo-second-order model were closer to those observed experimentally. Moreover, α, the initial rate constant of Elovich is larger than the desorption constant β, indicating a strong affinity between CR and the biochar surfaces.[11,18] However, for the biocomposite films, based on their error functions (R^2, RMSE and χ^2) we rather observed that the data are well fitted by the pseudo-second-order which often characterizes the chemisorption mechanism[56] and the Elovich model. Nevertheless, the similarity between the experimental q_e and those derived from the pseudo-first-order model also makes it suitable to describe the adsorption kinetics of CR on films, suggesting the involvement of the physisorption in the adsorption process.[57] This latter assertion is supported by the Elovich model, in which the desorption constant β is higher than the initial adsorption α, indicating that CR interacts weakly with the surface films.

To determine the rate-controlling step of the adsorption of the dye onto the prepared adsorbent materials, the kinetic data were analyzed with the Weber–Morris intra-particle diffusion model.[58] Since it was not possible to distinguish the two or three subdivisions corresponding to the different stages of the diffusion process, the fitted curves of the Weber–Morris intra-particle diffusion model showed a straight line (Fig. 6d–f) for all the films. This observation indicates that the multiple diffusion steps of the adsorption process are smoothly overlapped. In addition, the linear regression of the plots q_t *vs.* $t^{1/2}$ did not pass through the origin, resulting in the values of the boundary layer thickness constant C different from zero in all cases (Table S3), suggesting that the intra-particle diffusion was not the only controlling step for CR adsorption onto biocomposite films, as boundary layer diffusion also played a significant role in the process.[11] Due to their low R^2 (Table S3), the intra-particle diffusion model was not suitable to fit the kinetic data of the adsorption of CR onto the different biochars (BC, ABC and BBC). Due to their low adsorption capacities and the intervention of the filtration step in the experimental procedure, which significantly affected the time and the cost of treatment, the biochars were ignored and the experiments continued with biocomposite films only.

3.2.2. Adsorption isotherm studies. Fig. 7 shows the adsorption isotherms (q_e *vs.* C_e) of CR onto biocomposites. The adsorbed quantity, which increases with the initial CR concentration, can be attributed to the strong driving forces to overcome the mass transfer resistance from the bulk solution to the adsorbent surface induced by the concentration gradient.[59] In order to describe and understand the interaction between the CR and the biocomposites, the equilibrium data were analyzed

Table 2 Comparison of the Langmuir maximum adsorption capacity of congo red on different adsorbents at various experimental conditions

Adsorbents	pH	Temperature (°C)	Adsorbent dose (g L^{-1})	Concentration (mg L^{-1})	Type	Q_{max}	Ref.
Sugarcane bagasse	5	30	10	100–500	Powder	38.20	63
Polypyrrole modified nanocellulose	2	50	—	10–50	Powder	46.78	64
Activated carbon based-cocoa pod husks	2	50	1	20–100	Powder	43.67	65
Fe_3O_4@carbon@ZIF-8	4	RT[a]	3	30–1000	Powder	566.53	66
Eucalyptus wood sawdust	7	30	4	5–30	Powder	31.25	67
KOH-activated biochar	4	25	2	25–100	Powder	6.238	68
Fly ash	Natural	RT[a]	1	10–50	Powder	22.12	14
PANI@ZnO	5	25	0.4	50–200	Powder	69.82	69
Pine bark	Natural	25	10	5–100	Powder	3.92	5
Cellulose/chitosan hydrogel	—	25	2	10–70	Bead	40.00	70
Banana peel	7.9	30	1	10–120	Powder	18.20	71
Orange peel	7.9	30	1	10–120	Powder	14.00	71
Wastepaper nanocomposite	7	30	2	20–100	Membrane	71.00	9
Kaolin	3	30	1	20–60	Powder	5.41	15
Aspergillus niger	6	—	2.67	—	Powder	14.72	72
CH_1BC	**6.5**	**RT[a]**	**1**	**15–340**	**Film**	**48.95**	**This work**
CH_2BC						**55.26**	
CH_1ABC						**28.94**	
CH_2ABC						**44.72**	
CH_1BBC						**32.98**	
CH_2BBC						**62.23**	

[a] Room temperature.

using Langmuir, Freundlich, and Temkin isotherm models. According to the nonlinear fitting (Fig. 7) and the analysis of the corresponding error function values (higher R^2, and lower RMSE and χ^2) (Table S4), it is concluded that the Freundlich isotherm model adequately describes the adsorption process. This indicates that CR was adsorbed on a heterogeneous biocomposite surface with uniform adsorption energy by forming multilayers and leading to reversible adsorption suggesting that the physisorption was involved in the adsorption process.[29,60] Tan *et al.* (2021),[61] while using chitosan-modified inorganic nanowire membranes for CR removal, also found that the Freundlich model was the best for simulating CR adsorption. In addition, both the values of Freundlich exponent $1/n$ and the separation factor R_L calculated from the Langmuir constant (K_L) which are related to the favorability of the adsorption process were between 0 and 1 (Table S4), indicating that the adsorption of CR was favorable on all the biocomposites.[62] The Langmuir monolayer adsorption capacities (Table S4) within two biocomposite samples based on the same biochar increased with the increasing chitosan/biochar ratio increases with the highest value of 62.23 mg g^{-1} obtained for CH_2BBC, suggesting that the surface functional group (–NH_2 and –OH) play an important role in CR adsorption. Despite its low R^2 (0.810–0.889), the Temkin isotherm model may also indicate the involvement of electrostatic and π–π interactions between biocomposites and CR.[25]

The CR removal performance of the prepared biocomposite films was evaluated by comparing their Langmuir monolayer adsorption capacity with those of other reported materials listed in Table 2. In general, the biocomposite films exhibit high adsorption capacity. Their low-cost, environmentally friendly synthesis process, easy recovery, and facile regeneration allowing multiple reuse cycles as shown below, highlight their potential as promising adsorbent materials for CR remediation in aqueous solutions.

3.2.3. Effect of agitation speed. The agitation speed of the solution is a key factor in the adsorption process, as it affects the distribution of the adsorbate within the bulk solution and influences the formation of the outer peripheral boundary layer.[73] The results of the agitation speed of the CR solution and the biofilms are given in Fig. 8a. From this figure, it can be seen that increasing the agitation speed from 0 to 320 rpm favors the adsorption of CR molecules on the films. In fact, increasing the agitation speed significantly reduces the resistance of the outer boundary layer thickness, which favors the transfer of CR molecules from the bulk solution to the surface of the films (adsorbent). This occurs because the CR molecules are pushed toward the film surface by the increase in turbulence and the

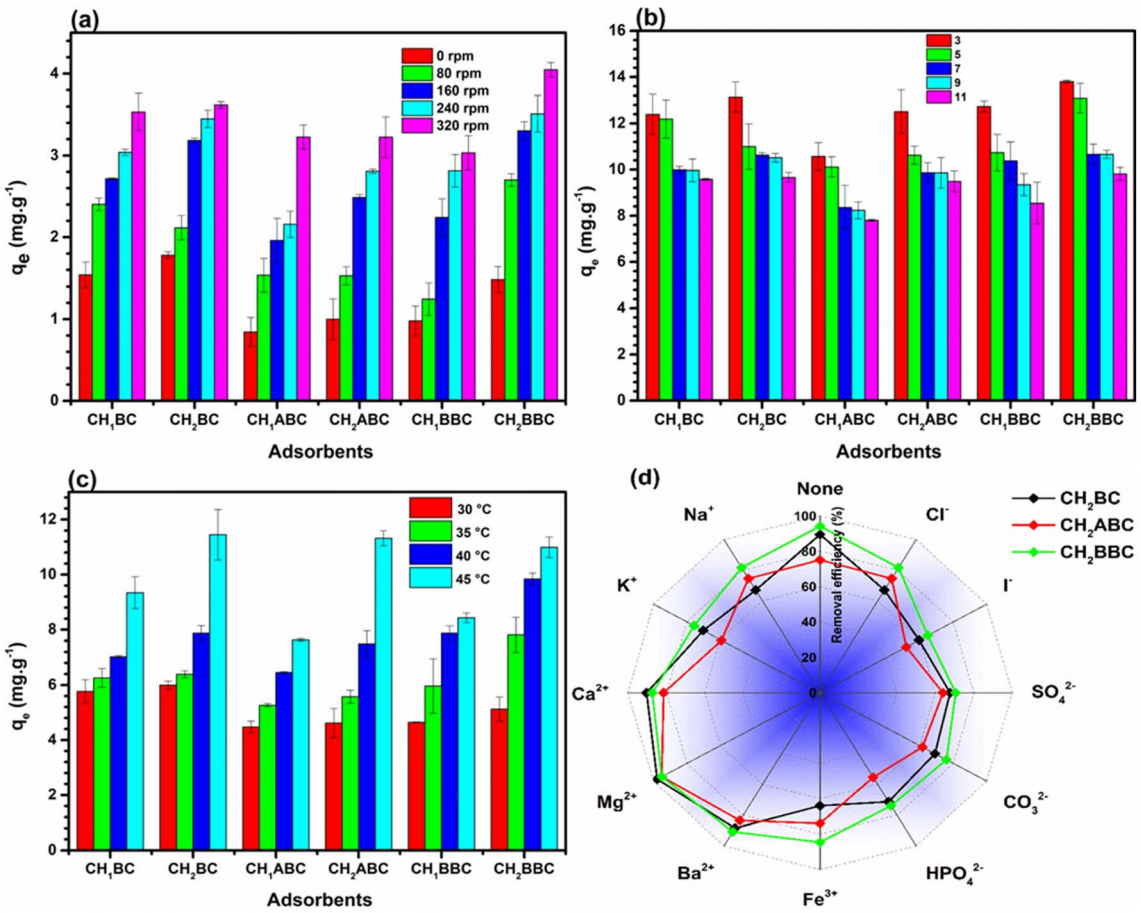

Fig. 8 Effect of (a) agitation seep ($[CR]_0 = 15$ mg L^{-1}, RT, $t = 60$ min, pH 6.5), (b) pH ($[CR]_0 = 15$ mg L^{-1}, RT, $t = 24$ h, 320 rpm), (c) temperature ($[CR]_0 = 15$ mg L^{-1}, $t = 60$ min, pH 6.5, 320 rpm), and (d) interfering ions ($[CR]_0 = [ion] = 15$ mg L^{-1}, RT, $t = 24$ h, pH 6.5, 320 rpm).

dissipation of energy generated in the agitation area, increasing the external mass transfer of CR into the adsorbent active sites.[60,74]

3.2.4. Effect of pH. Fig. 8b shows that for all the films, the maximum amount of CR adsorbed was obtained at the initial pH of 3. CH_2BBC shows the highest q_e of ~14 mg g^{-1} which decreases continuously with increasing pH, reaching the value of ~10 mg g^{-1} at pH 11. These observations are related to two main parameters including the ionized structure of the CR and the surface chemistry of the adsorbent. At pH > 5.5 the red color of the anionic form of CR is observed while at pH < 5.5, it is predominantly in its protonated form (blue), which consists of two tautomeric and one azoic form (Scheme 1). Moreover, Scheme 1 shows that the azo group (–N=N–) present in the CR molecule is the most affected by the pH variation, leaving the sulfonate group ($-SO_3^-$) unprotonated,[2,3] which would thus be the most reactive site for the adsorption process.[13] Regarding the adsorbents, added to the surface functional groups discussed by XPS and FTIR, the pH_{pzc} evaluated by the drift method[75] were found to be approximately in the range of 6.27–7.08 (Table 1 and Fig. S7). Therefore, at pH < pH_{pzc}, the surface charges of the films are dominated by positive charges and *vice versa*. Under strongly acidic conditions, most of the surface functional groups (–NH_2, –COOH, and –OH) are protonated due to the availability of more protons in the solution, resulting in a high electrostatic attraction of the sulfonate group ($-SO_3^-$), leading to higher adsorption capacities at pH 3. With increasing pH, the surface becomes less and less protonated until the pH > pH_{pzc}, where the surface becomes negatively charged, reducing the adsorption capacity due to less electrostatic attraction. In addition, the presence of hydroxyl ions in the solution at higher pH may compete with CR for adsorption sites. At a high pH range, the adsorption of CR onto films was still effective, indicating that other interactions (*e.g.*, H-bonding, n–π and π–π stacking), besides electrostatic attraction, were involved in the adsorption mechanisms of CR.[76]

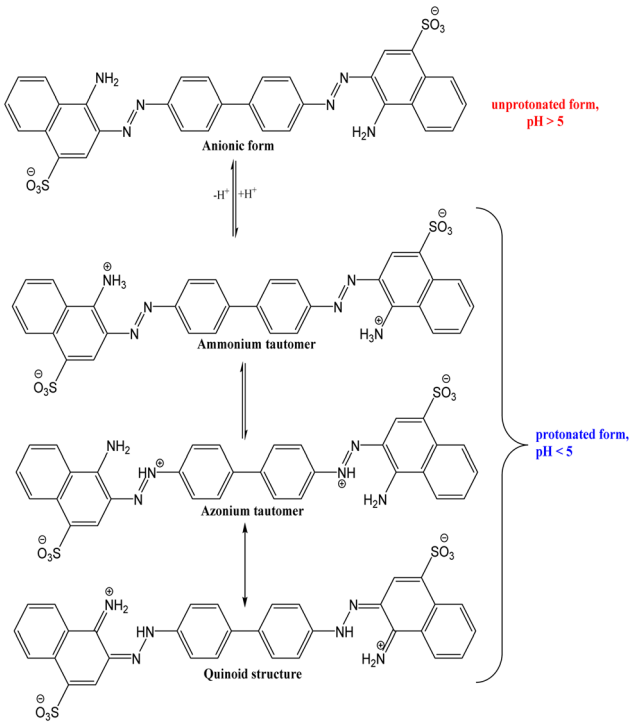

Scheme 1 Illustration of the effect of pH on the structure of CR.

3.2.5. Effect of temperature and thermodynamic. As shown in Fig. 8c, the adsorption capacities of all the biofilms increase with increasing temperature, with a particular increase in the uptake performance of CH_1BC, CH_2BC, and CH_2ABC from 30 °C to 45 °C, indicating that they are much more efficient at high temperature compared to others, suggesting the endothermic process of the adsorption. These observations can be attributed to phenomena such as the swelling of the adsorbent with rising temperature which leads to pore expansion and large exposure of the adsorption sites for CR.[77] On the other hand, the rising temperature may increase the kinetic energy of CR leading to more collisions with the surface of the films, thus increasing the adsorption.[78] The thermodynamics of CR sorption onto the prepared biofilms was evaluated using the Gibbs–Helmholtz equation. The van't Hoff plots related to the CR sorption on all films (Fig. S8) were used to determine the thermodynamic parameters summarized in Table S5. For CH_1ABC, the values of $\Delta G°$ were all positive, indicating that the adsorption process of CR on CH_1ABC was unfavorable and nonspontaneous. This explains, among other things, why CH_1ABC has the lowest adsorption capacity. However, for the other adsorbents, the adsorption process becomes more spontaneous and favorable ($\Delta G° < 0$) with increasing temperature, especially particularly for CH_2BBC from which the $\Delta G°$ became negative at 308 K. The positive values of $\Delta H°$ confirm the endothermic character of the adsorption process. The adsorption mechanism of CR onto the films can also be elucidated from the magnitude of $\Delta H°$. Indeed, in the range of 0.4–80 kJ mol^{-1}, the adsorption mechanism is dominated by physisorption, while in the range of 200–800 kJ mol^{-1}, chemisorption predominates.[79] In the present study, the magnitude of $\Delta H°$ is between ~48 and ~94 kJ mol^{-1}, indicating that the adsorption mechanism of CR onto film is controlled by physisorption. The positive value of $\Delta S°$ suggested that at the liquid–solid interface, there is an increase in disorder and randomness during the adsorption process of CR onto films.[80]

3.2.6. Interfering ions. Industrial textile dyeing effluents typically contain dissolved inorganic ions such as Cl^-, I^-, SO_4^{2-}, CO_3^{2-}, HPO_4^{2-}, Na^+, K^+, Ca^{2+}, Mg^{2+}, Fe^{2+}, and Ba^{2+}. These ions are present in auxiliaries used as acidifiers, catalysts, dispersing agents, and electrolytes,[25] which may influence the dye removal process. As shown in Fig. 8d, the presence of interfering ions significantly affects the uptake of CR by biofilm. Due to their negative charges, the anions compete with CR containing the sulfonate groups ($-SO_3^-$) for adsorption sites (–NH_2 and –OH), leading to a reduction in CR removal efficiency.[64] The prominence of that reduction in the presence of I^- may be due, in addition to the aforementioned competition, to the formation of complex molecules in solution that reduce the amount of free CR for adsorption. The increase in CR removal efficiency in the presence of Ca^{2+}, Ba^{2+}, and Mg^{2+} was not only attributed to the

sorption phenomenon. Indeed, during the experiments, we observed that the addition of multivalent cations (Ca^{2+}, Ba^{2+}, Mg^{2+}, and Fe^{3+}) to the CR solution led to the reduction of the concentration of this later before adsorption, which may be attributed to the formation of a complex/precipitate as mentioned in some reported works.[81,82] Although there was a reduction in the concentration of CR in the presence of Fe^{3+}, the removal efficiency decreased due to the presence of a large amount of Cl^- in the solution. K^+ did not affect the initial CR concentration, but may interact with $-SO_3^-$ through electrostatic interactions, reducing the number of free $-SO_3^-$ available for reaction with surface functional groups of films ($-NH_2$ and –OH). From this study, despite the slight antagonistic effect of the co-existing ions, the biocomposite films could be efficiently used for organic dye sequestration from an aqueous solution.

3.2.7. CR adsorption mechanism. The SEM image of CH_2BBC after CR adsorption shows that there is no significant change in the morphology (Fig. S9), indicating that the

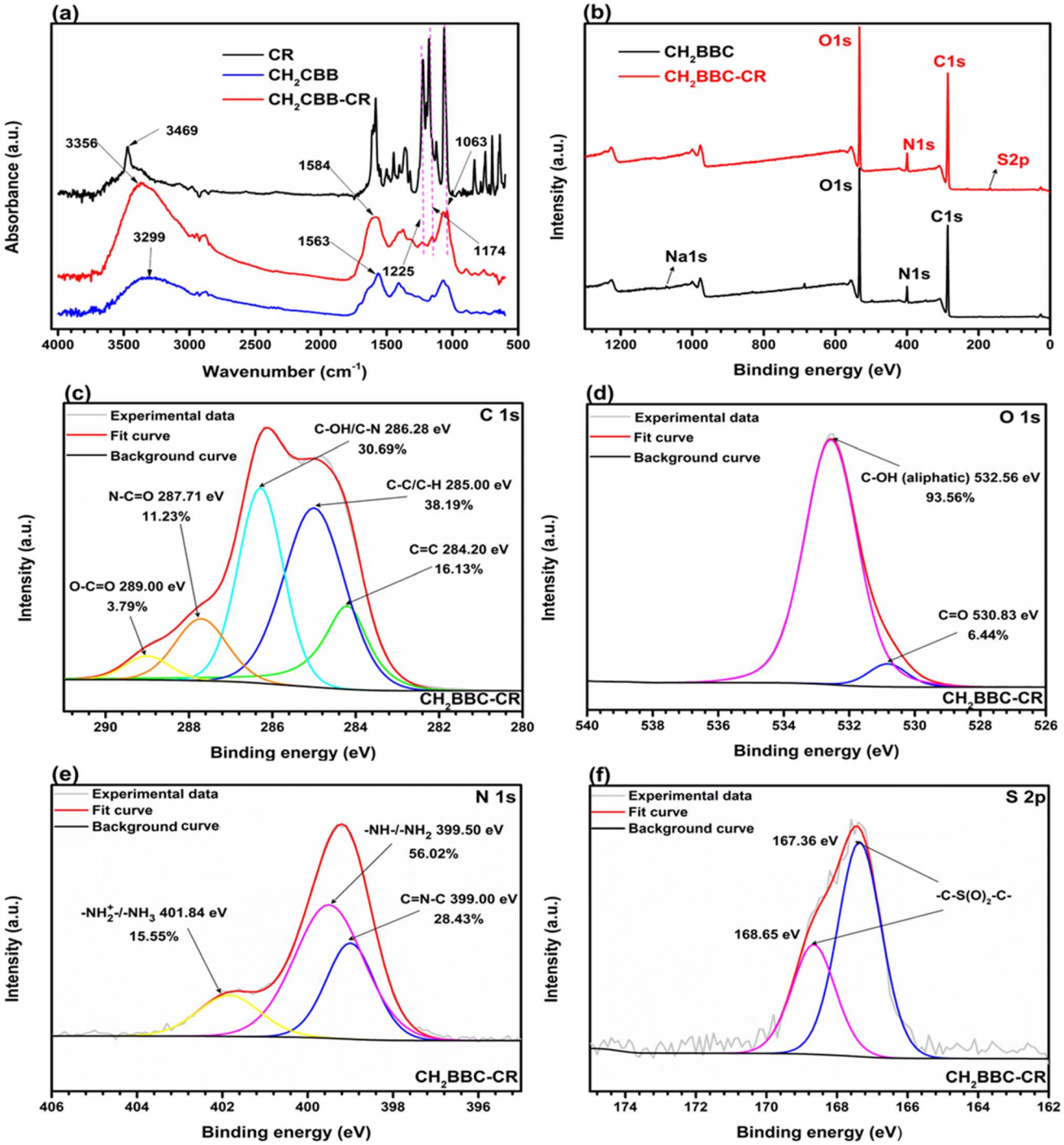

Fig. 9 FTIR spectra (a), XPS full scan (b), and high-resolution spectra of C 1s (c), O 1s (d), N 1s (e), and S 2p (f).

adsorption of CR did not alter the surface of the film due to its high stability. On the other hand, the elemental analysis derived from EDS and XPS (Tables S1 and S2) shows a significant increase in carbon content and a decrease in oxygen content after adsorption, indicating that CR was successfully adsorbed on the surface of CH_2BBC.

The appearance of the peaks at about 1225, 1174, and 1063 cm^{-1} respectively assigned to C–N, S–O, and S=O vibrations in the CR molecule[4] on the biocomposite after adsorption (Fig. 9a) indicated that the dye was adsorbed on the surface of biocomposite. The narrowing and intensification of the –NH/–OH joint band centered at 3362 cm^{-1} on the biocomposite after CR adsorption indicated the formation of H-bonding between the –NH/–OH of CH_2BBC and $-NH_2$ of CR.[19] The peak at 1563 cm^{-1} on CH_2BBC which was assigned to the C=C (aromatic) vibration shifted to 1584 cm^{-1} after CR adsorption indicating the π–π interaction between the aromatic ring of the dye and that of the film derived from BC.[75]

Two main features were observed on the XPS spectrum full scan of CH_2BBC-CR (Fig. 9b): (1) the rising of a peak attributed to S 2p attributed to sulfur present in CR molecule and clearly indicated that it was immobilized on the surface of CH_2BBC, and (2) the disappearance of the Na 1s peak indication the occurrence of ion exchange between –COONa and CR.[25] Moreover, in the high-resolution spectrum, we noticed a variation in peak intensities and movement of the binding energy of C 1s, O 1s, and N 1s indicating/confirming the change of the surface chemistry of CH_2BBC after CR adsorption. The deconvoluted peak of C 1s (Fig. 9c) revealed that the content of C–C/C–H and C=C increased indicating that a large amount of CR was adsorbed onto the surface of CH_2BBC.[83] The reductions of C–O/C–N content from 51.44 to 30.69% and that of N–C=O from 12.79 to 11.23% indicated their contribution to CR removal which may be through H-bonding.[83,84] The increase (from 3.14 to 3.79%) of O–C=O content after adsorption may be due to the reaction between N–C=O (–COOH) of CH_2BBC and the

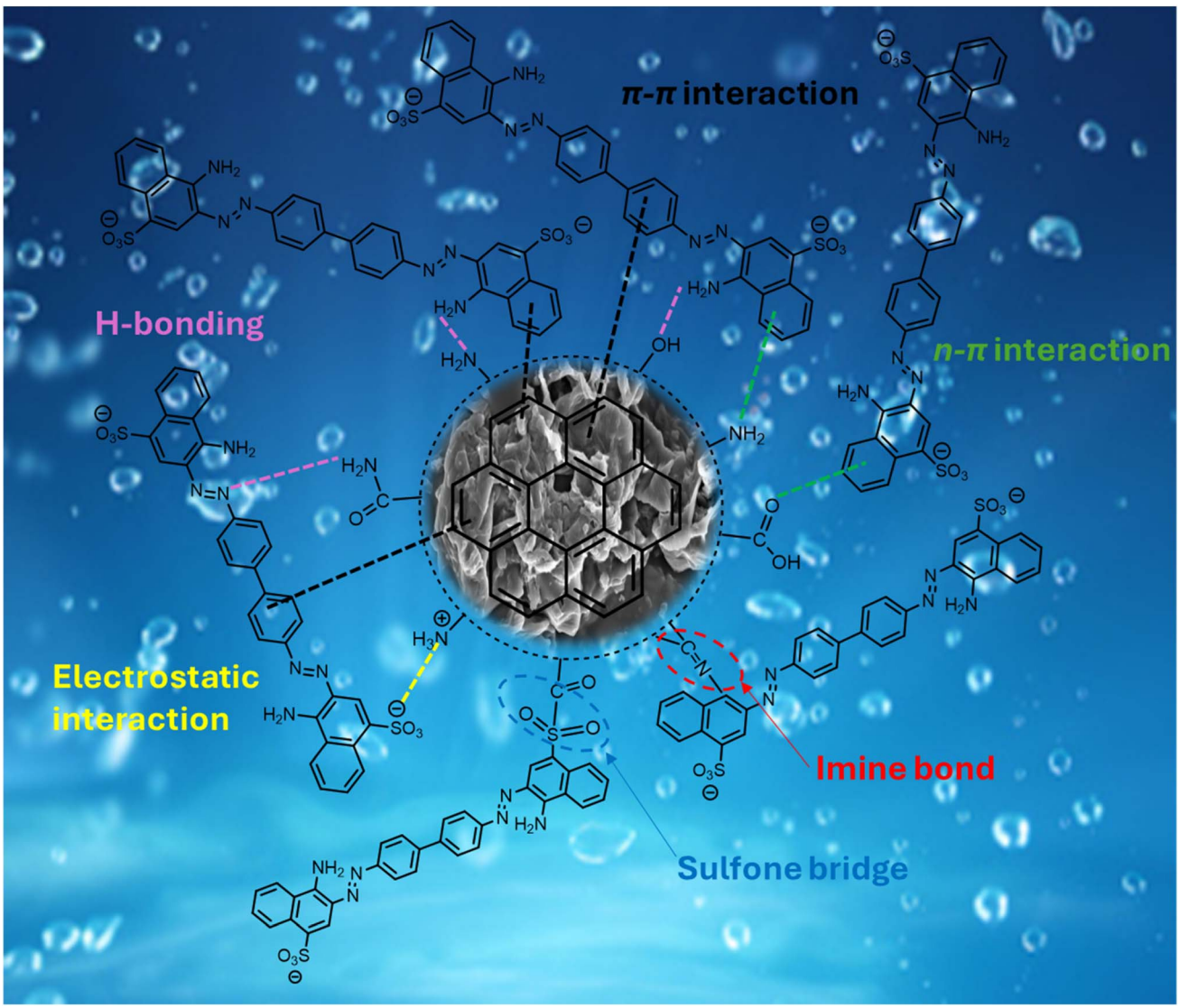

Fig. 10 Proposed adsorption mechanism of CR onto chitosan–biochar biocomposite film.

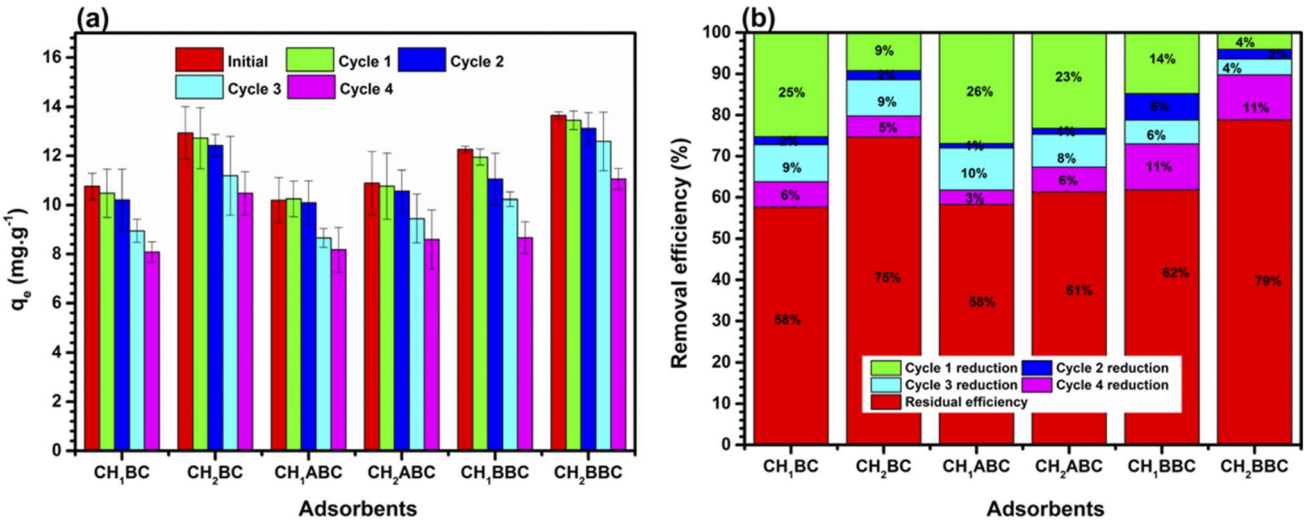

Fig. 11 Reusability of biofilms (a) and reduction efficiency after each adsorption–desorption cycle (b).

sulfonate group of CR.[85] On O 1s spectra (Fig. 9d), the increase in the percentage of –OH from 86.59 to 93.56% may correlated to the interaction between $-SO_3^-$ and the protonated functions of CH_2BBC. The C=O content significantly decreases from 13.41 to 6.44% due to the sharing of free electron pair bond of O with CR through n–π interactions.[66] This reduction may also be due to the reaction between C=O (carbonyl) of CH_2BBC and $-NH_2$ of CR to form an imine function as confirmed by the increase of the C=N–C fraction from 8.57 to 28.43% in N 1s spectra (Fig. 9e), which among other things, contributes to confirm the chemisorption hypothesis presented above. The $-NH_2$ present on the film may be involved in some interactions with CR including H-bonding, n–π (π electron of the CR benzene ring), confirmed by the slight increase of $-NH_2^+$–/–NH_3^+. The S 2p peak after deconvolution was split into two (Fig. 9f) centered at 168.68 and 167.36 eV attributed to the sulfone bridge (–C–S(O)$_2$–C–) between the CR and CH_2BBC.[86] Although the study of the effect of pH revealed the importance of the electrostatic interactions, additional investigations using zeta potential–pH would be valuable to strengthen this assertion. The overall mechanism of CR adsorption onto biocomposite is illustrated in Fig. 10.

3.2.8. Regeneration and reusability. Desorption and reusability experiments were conducted to evaluate the stability and efficiency of films after multiple adsorption–desorption cycles to provide insight into a practical potential repeated use. It was shown above that the adsorption mechanism could be governed by hydrogen bonding, chemical reaction, and electrostatic attraction between the surface functional groups of the biocomposite film, sulfonate, and nitrogen-containing groups of CR. The NaOH solution easily broke these interactions, thereby promoting desorption.[1] As expected, the adsorption capacities of the different films decreased after four adsorption–desorption cycles (Fig. 11a). The biocomposites with high biochar content lost significant adsorption capacity after the first cycle (CH_1BC: 25%; CH_1ABC: 26%; and CH_1BBC: 14%) (Fig. 11b). This could be due to: (i) some CR molecules being trapped by the biochar particles present in the composites through the mechanism of chemisorption (*i.e.* the formation of imine and sulfone bridges, as shown by the XPS after adsorption) which leads to the progressive occupation of active sites;[87] (ii) pore filling/blockage, which reduces the accessibility of adsorption sites;[88] or (iii) partial alteration of surface functional groups and the texture of films occurring during the cycling process.[49] Nevertheless, CH_2BC and CH_2BBC retained ~75% and ~79% of their adsorption capacities after four adsorption–desorption cycles, respectively, highlighting their strong potential for practical applications.

It is important to note that the main objective of the desorption process is to regenerate the adsorbent and transfer the pollutant from the solid phase to a smaller volume of the liquid phase. This concentrates the pollutant. To address the eventual question of the fate of the concentrated desorbed solution containing CR and NaOH, further treatment is required. This treatment could be an advanced oxidation process or electrochemical degradation. This would ensure complete mineralization of the CR before discharged into the environment.[89]

4. Conclusion

In the present study, the authors discussed the preparation and extensive characterization of novel biocomposite films based on pristine, HNO_3-, and KOH-modified biochar and glutaraldehyde-crosslinked chitosan, which were applied for the removal of congo red from aqueous solution. Despite their low porosity, the biocomposite films exhibited a rich surface chemistry with oxygenated and aminated groups favorable for CR uptake. Their excellent mechanical strength enabled easy separation and reuse without filtration, offering a significant advantage over the powder adsorbents. Among the prepared adsorbent materials, the biocomposite film derived from KOH-treated biochar with a chitosan–BBC ratio of 2 : 1 (CH_2BBC) achieved the highest adsorption capacity (62.23 mg g^{-1}). A

comprehensive study of the effect of pH, kinetics, isotherms, and thermodynamics supported by the results of SEM-EDS, FTIR, and XPS of CH_2BBC after CR adsorption revealed that multiple interactions, including electrostatic attraction, π–π stacking, H-bonding, n–π interaction, and sulfone bridging, governed the adsorption mechanism. CH_2BBC retained up to 79% of its adsorption after four consecutive adsorption–desorption cycles, highlighting its strong reusability potential for CR removal from aqueous solution. In addition, these biocomposite films need to be tested in real wastewater effluents to evaluate their applicability for industrial-scale applications.

Author contributions

René Blaise Ngouateu Lekene: conceptualization, methodology, investigation, writing – original draft, funding acquisition; Mária Kováčová: investigation, resources; Christian Brice Dantio Nguela: writing – review and editing; Matej Mičušík: resources, investigation, data curation; Alena Opálková Šišková: investigation, resources; Anna Vykydalová: resources, investigation; Hamed Peidayesh: resources, investigation, data curation; Daouda Kouotou: resources, writing – review and editing, Peter Machata: resources, investigation, data curation; Ndi Juluis Nsami: resources, writing – review and editing; Angela Kleinová: investigation, resources; Julien Parmentier: writing – review and editing; Zdenko Špitalský: supervision, writing – review and editing, funding acquisition.

Conflicts of interest

There are no conflicts to declare.

Data availability

The data supporting this article have been included as part of the supplementary information (SI). Supplementary information is available. See DOI: https://doi.org/10.1039/d6ra01186a.

Acknowledgements

René Blaise Ngouateu Lekene thanks the National Scholarship Programme (NSP) of the Slovak Republic for the financial support of his stay at the Polymer Institute, Slovak Academy of Sciences, and Dr Cyrille Vaulot (IS2M-CNRS) for N_2 adsorption–desorption.

References

1 N. El Messaoudi, M. El Khomri, N. Chlif, Z. G. Chegini, A. Dbik, S. Bentahar and A. Lacherai, *Groundw. Sustain. Dev.*, 2021, **12**, 100552.
2 E. Pigorsch, A. Elhaddaoui and S. Turrell, *Spectrochim. Acta, Part A*, 1994, **50**, 2145–2152.
3 K. Csillag, T. Emri, D. E. N. Rangel and I. Pócsi, *Fungal Biol.*, 2023, **127**, 1180–1186.
4 R. Kaur and H. Kaur, *Port. Electrochim. Acta*, 2016, **34**, 185–196.
5 K. Litefti, M. S. Freire, M. Stitou and J. González-Álvarez, *Sci. Rep.*, 2019, **9**, 16530.
6 N. F. Zainudin, S. T. Sam, Y. S. Wong, H. Ismail, S. Walli, K. Inoue, G. Kawamura and W. K. Tan, *Polymers*, 2023, **15**, 237.
7 P. O. Oladoye, M. O. Bamigboye, O. D. Ogunbiyi and M. T. Akano, *Groundw. Sustain. Dev.*, 2022, **19**, 100844.
8 R. R. M. Khan, H. Qamar, A. Hameed, A. ur Rehman, M. Pervaiz, Z. Saeed, A. Adnan and A. R. Ch, *Water, Air, Soil Pollut.*, 2022, **233**, 468.
9 R. Goswami, A. Mishra, A. Mirza, W. Ahmad and R. Rana, *J. Appl. Polym. Sci.*, 2024, **141**, e56275.
10 F. Mashkoor and A. Nasar, *J. Magn. Magn. Mater.*, 2020, **500**, 166408.
11 G. Agbor Tabi, L. Ngouateu Rene Blaise, K. Daouda, A. Naphtali Odogu, A. Aime Victoire, N. Nsami Julius and K. Joseph Mbadcam, *Arabian J. Chem.*, 2022, **15**, 103515.
12 H. Li, V. L. Budarin, J. H. Clark, M. North and X. Wu, *J. Hazard. Mater.*, 2022, **436**, 129174.
13 F. B. D. Saïah and N. Bettahar, *Desalin. Water Treat.*, 2022, **254**, 260–273.
14 M. Harja, G. Buema and D. Bucur, *Sci. Rep.*, 2022, **12**, 6087.
15 T. A. Aragaw and A. N. Alene, *Emerging Contam.*, 2022, **8**, 59–74.
16 T. Panczyk, P. Wolski, A. Jagusiak and M. Drach, *RSC Adv.*, 2014, **4**, 47304–47312.
17 J. Lu, C. Zhang, J. Wu and Y. Luo, *Water, Air, Soil Pollut.*, 2017, **228**, 327.
18 R. B. N. Lekene, T. M. M. Ntep, M. N. A. Fetzer, T. Strothmann, J. N. Nsami and C. Janiak, *Environ. Sci. Pollut. Res.*, 2023, **30**, 100095–100113.
19 X. Huang, F. Yu, Q. Peng and Y. Huang, *RSC Adv.*, 2018, **8**, 29781–29788.
20 J. Wang and M. Zhang, *Int. J. Environ. Res. Public Health*, 2020, **17**, 1075.
21 N. Somsesta, V. Sricharoenchaikul and D. Aht-Ong, *Mater. Chem. Phys.*, 2020, **240**, 122221.
22 J. Desbrieres and E. Guibal, *Polym. Int.*, 2018, **67**, 7–14.
23 J. O. Gonçalves, M. M. Strieder, L. F. O. Silva, G. S. Dos Reis and G. L. Dotto, *Int. J. Biol. Macromol.*, 2024, **270**, 132307.
24 A. H. Jawad, A. S. Abdulhameed, L. D. Wilson, M. A. K. M. Hanafiah, W. I. Nawawi, Z. A. ALOthman and M. Rizwan Khan, *J. Polym. Environ.*, 2021, **29**, 2855–2868.
25 X. Su, X. Wang, Z. Ge, Z. Bao, L. Lin, Y. Chen, W. Dai, Y. Sun, H. Yuan, W. Yang, J. Meng, H. Wang and S. C. Pillai, *Chem. Eng. J.*, 2024, **486**, 150387.
26 J. Song, S. A. Messele, L. Meng, Z. Huang and M. Gamal El-Din, *Water Res.*, 2021, **194**, 116930.
27 H. Chen, Y. Gao, A. El-Naggar, N. K. Niazi, C. Sun, S. M. Shaheen, D. Hou, X. Yang, Z. Tang, Z. Liu, H. Hou, W. Chen, J. Rinklebe, M. Pohořelý and H. Wang, *J. Hazard. Mater.*, 2022, **425**, 127971.
28 Y. Huang, X. Lee, M. Grattieri, M. Yuan, R. Cai, F. C. Macazo and S. D. Minteer, *Chem. Eng. J.*, 2020, **380**, 122375.
29 R. B. N. Lekene, N. O. Ankoro, D. Kouotou, G. B. N. Yemeli, S. A. Benedoue, J. N. Nsami and J. K. Mbadkam, *Biomass*

Convers. Biorefin., 2024, **14**, 20855–20872, DOI: 10.1007/s13399-023-04239-0.
30 J. Liu, B. Zhou, H. Zhang, J. Ma, B. Mu and W. Zhang, *Bioresour. Technol.*, 2019, **294**, 122152.
31 V. Son Tran, H. Hao Ngo, W. Guo, T. Ha Nguyen, T. Mai Ly Luong, X. Huan Nguyen, T. Lan Anh Phan, V. Trong Le, M. Phuong Nguyen and M. Khai Nguyen, *Bioresour. Technol.*, 2023, **385**, 129384.
32 A. J. Asuquo, X. Zhang, L. Lin and J. Li, *Int. J. Green Energy*, 2024, **21**, 2218–2227.
33 J. Ndi Nsami and J. Ketcha Mbadcam, *J. Chem.*, 2013, **2013**, 469170.
34 V. Rizzi, D. Lacalamita, J. Gubitosa, P. Fini, A. Petrella, R. Romita, A. Agostiano, J. A. Gabaldón, M. I. Fortea Gorbe, T. Gómez-Morte and P. Cosma, *Sci. Total Environ.*, 2019, **693**, 133620.
35 Z. Wang, J. Li, G. Zhang, Y. Zhi, D. Yang, X. Lai and T. Ren, *Materials*, 2020, **13**, 2270.
36 B. Hayati and N. M. Mahmoodi, *Desalin. Water Treat.*, 2012, **47**, 322–333.
37 M. C. Collivignarelli, W. A. M. A. N. Illankoon, C. Milanese, S. Calatroni, F. M. Caccamo, M. Medina-Llamas, A. Girella and S. Sorlini, *Water*, 2024, **16**, 698.
38 R. B. N. Lekene, D. Kouotou, N. O. Ankoro, A. P.-M. S. Kouoh, J. N. Ndi and J. M. Ketcha, *J. Saudi Chem. Soc.*, 2021, **25**, 101316.
39 Y. Xue, W. Cheng, M. Cao, J. Gao, J. Chen, Y. Gui, W. Zhu and F. Ma, *Environ. Sci. Pollut. Res.*, 2022, **29**, 77536–77552.
40 M. Thommes, K. Kaneko, A. V. Neimark, J. P. Olivier, F. Rodriguez-Reinoso, J. Rouquerol and K. S. W. Sing, *Pure Appl. Chem.*, 2015, **87**, 1051–1069.
41 R. B. N. Lékéné, J. N. Nsami, A. Rauf, D. Kouotou, P. D. B. Belibi, M. I. Bhanger and J. K. Mbadcam, *Am. J. Anal. Chem.*, 2018, **09**, 439.
42 İ. Teğin, S. Öc and C. Saka, *Biomass Convers. Biorefin.*, 2025, **15**, 6805–6816, DOI: 10.1007/s13399-024-05477-6.
43 M. Monier, D. M. Ayad, Y. Wei and A. A. Sarhan, *React. Funct. Polym.*, 2010, **70**, 257–266.
44 J. K. Fatombi, E. A. Idohou, S. A. Osseni, I. Agani, D. Neumeyer, M. Verelst, R. Mauricot and T. Aminou, *Fibers Polym.*, 2019, **20**, 1820–1832.
45 Y. Zhou, B. Gao, A. R. Zimmerman, J. Fang, Y. Sun and X. Cao, *Chem. Eng. J.*, 2013, **231**, 512–518.
46 M. C. Biesinger, *Appl. Surf. Sci.*, 2022, **597**, 153681.
47 S. Ge, S. Wang, W. Mai, K. Zhang, M. Tanveer, L. Wang and C. Tian, *Environ. Sci. Pollut. Res.*, 2023, **30**, 66113–66124.
48 L. Zhang, S. C. Jiang and Y. Guan, *Environ. Res.*, 2021, **194**, 110667.
49 Y. Yu, W. Liu, Y. Zhang, B. Zhang, Y. Jin, S. Chen, S. Tang, Y. Su, X. Yu and G. Chen, *Arabian J. Chem.*, 2024, **17**, 105746.
50 H. Kandil, A. E. Abdelhamid, R. M. Moghazy and A. Amin, *Polym. Eng. Sci.*, 2022, **62**, 145–159.
51 H. Zeng, H. Hao, X. Wang and Z. Shao, *Int. J. Biol. Macromol.*, 2022, **213**, 369–380.
52 M.-X. Huo, Y.-L. Jin, Z.-F. Sun, F. Ren, L. Pei and P.-G. Ren, *Carbohydr. Polym.*, 2021, **254**, 117473.
53 V. Rizzi, J. Gubitosa, P. Fini, R. Romita, S. Nuzzo, J. A. Gabaldón, M. I. F. Gorbe, T. Gómez-Morte and P. Cosma, *J. Environ. Sci. Health, Part A: Toxic/Hazard. Subst. Environ. Eng.*, 2020, 1–12.
54 A. Kwaśniewska, M. Świetlicki, A. Prószyński and G. Gładyszewski, *Polymers*, 2021, **13**, 4406.
55 J. Wang, X. Sun, H. Zhang, M. Dong, L. Li, H. Zhangsun and L. Wang, *Food Hydrocolloids*, 2022, **124**, 107258.
56 Y. S. Ho and G. McKay, *Process Biochem.*, 1999, **34**, 451–465.
57 E. D. Revellame, D. L. Fortela, W. Sharp, R. Hernandez and M. E. Zappi, *Clean Eng. Technol.*, 2020, **1**, 100032.
58 W. J. Weber and J. C. Morris, *J. Sanit. Eng. Div., Am. Soc. Civ. Eng.*, 1963, **89**, 31–59.
59 G. Y. Boris, A. N. Odogu, L. N. R. Blaise, K. Daouda, N. J. Nsami, N. H. Manga and K. J. Mbadcam, *J. Mater. Sci. Chem. Eng.*, 2023, **11**, 75–105.
60 J. Gubitosa, V. Rizzi, P. Fini, S. Nuzzo and P. Cosma, *Int. J. Mol. Sci.*, 2023, **24**, 8552.
61 Y. Tan, Y. Kang, W. Wang, X. Lv, B. Wang, Q. Zhang, C. Cui, S. Cui, S. Jiao, G. Pang and S. Feng, *Appl. Surf. Sci.*, 2021, **569**, 150970.
62 A. Naphtali Odogu, K. Daouda, L. Paul Keilah, G. Agbor Tabi, L. Ngouateu Rene, N. Julius Nsami and K. Josoph Mbadcam, *Arabian J. Chem.*, 2020, **13**, 5241–5253.
63 Z. Zhang, L. Moghaddam, I. M. O'Hara and W. O. S. Doherty, *Chem. Eng. J.*, 2011, **178**, 122–128.
64 T. Shahnaz, S. Mohamed Madhar Fazil, V. C. Padmanaban and S. Narayanasamy, *Int. J. Biol. Macromol.*, 2020, **151**, 322–332.
65 M. O. Olakunle, A. A. Inyinbor, A. O. Dada and O. S. Bello, *Int. J. Sustain. Eng.*, 2018, **11**, 4–15.
66 Z. Xiong, H. Zheng, Y. Hu, X. Hu, W. Ding, J. Ma and Y. Li, *Sep. Purif. Technol.*, 2021, **277**, 119053.
67 V. S. Mane and P. V. Vijay Babu, *J. Taiwan Inst. Chem. Eng.*, 2013, **44**, 81–88.
68 N. Kaya, Z. Yıldız Uzun, C. Altuncan and H. Uzun, *Biomass Convers. Biorefin.*, 2022, **12**, 5293–5315, DOI: 10.1007/s13399-021-01856-5.
69 I. Toumi, H. Djelad, F. Chouli and A. Benyoucef, *J. Inorg. Organomet. Polym.*, 2022, **32**, 112–121.
70 M. Li, Z. Wang and B. Li, *Desalin. Water Treat.*, 2016, **57**, 16970–16980.
71 G. Annadurai, R.-S. Juang and D.-J. Lee, *J. Hazard. Mater.*, 2002, **92**, 263–274.
72 Y. Fu and T. Viraraghavan, *Adv. Environ. Res.*, 2002, **7**, 239–247.
73 G. L. Dotto and L. A. A. Pinto, *J. Hazard. Mater.*, 2011, **187**, 164–170.
74 M. R. Islam and M. G. Mostafa, *Sustain. Water Resour. Manag.*, 2022, **8**, 52.
75 Y. M. Correa-Navarro, J. C. Moreno-Piraján and L. Giraldo, *Braz. J. Chem. Eng.*, 2022, **39**, 933–948.
76 Y. Dago-Serry, K. N. Maroulas, A. K. Tolkou, N. AbdelAll, A. N. Alodhayb, G. A. Khouqeer and G. Z. Kyzas, *J. Mol. Struct.*, 2024, **1298**, 137044.

77 Z. Zeng, S. Ye, H. Wu, R. Xiao, G. Zeng, J. Liang, C. Zhang, J. Yu, Y. Fang and B. Song, *Sci. Total Environ.*, 2019, **648**, 206–217.
78 S. Dong, Y. Wang, Y. Zhao, X. Zhou and H. Zheng, *Water Res.*, 2017, **126**, 433–441.
79 Y. Wang, C. Wang, X. Huang, Q. Zhang, T. Wang and X. Guo, *Chemosphere*, 2024, **349**, 140736.
80 D. Akin Sahbaz, *Polymers*, 2023, **15**, 3246.
81 N. J. Hahn, *Can. J. Microbiol.*, 1966, **12**, 725–733.
82 G. Han, Y. Du, Y. Huang, W. Wang, S. Su and B. Liu, *Chemosphere*, 2022, **289**, 133109.
83 C. Zhang, L. Meng, Z. Fang, Y. Xu, Y. Zhou, H. Guo, J. Wang, X. Zhao, S. Zang and H. Shen, *Molecules*, 2024, **29**, 4517.
84 Y. Liang, X. Xu, F. Yuan, Y. Lin, Y. Xu, Y. Zhang, D. Chen, W. Wang, H. Hu and J. Z. Ou, *Carbon*, 2023, **205**, 40–53.
85 X. Zhang, F. Li, X. Zhao, J. Cao, S. Liu, Y. Zhang, Z. Yuan, X. Huang, C. F. De Hoop, X. Peng and X. Huang, *Gels*, 2023, **9**, 40.
86 L. Qie, W. Chen, X. Xiong, C. Hu, F. Zou, P. Hu and Y. Huang, *Adv. Sci.*, 2015, **2**, 1500195, DOI: 10.1002/advs.201500195.
87 D. Li, H. Zhang, K. Ren, D. Zhu, G. Xiao, M. Vakili, W. Wang and J. Ye, *Sep. Purif. Technol.*, 2025, **361**, 131305.
88 M. Turk Sekulic, N. Boskovic, A. Slavkovic, J. Garunovic, S. Kolakovic and S. Pap, *Process Saf. Environ. Prot.*, 2019, **125**, 50–63.
89 S. Mehmood, W. Ahmed, M. Rizwan, J. Bundschuh, A. S. M. Elnahal and W. Li, *Sep. Purif. Technol.*, 2025, **361**, 131305.